

The calibration of a laser profiling system for seafloor micro-topography measurements

Kathryn R. Loeffler and Nicholas P. Chotiros*

Applied Research Laboratories, The University of Texas at Austin, P.O. Box 8029, Austin, TX 78713-8029, USA

(Received March 14, 2011, Accepted July 14, 2011)

Abstract. A method for calibrating a laser profiling system for seafloor micro-topography measurements is described. The system consists of a digital camera and an arrangement of six red lasers that are mounted as a unit on a remotely operated vehicle (ROV). The lasers project as parallel planes onto the seafloor, creating profiles of the local topography that are interpreted from the digital camera image. The goal of the calibration was to determine the plane equations for the six lasers relative to the camera. This was accomplished in two stages. First, distortions in the digital image were corrected using an interpolation method based on a virtual pinhole camera model. Then, the laser planes were determined according to their intersections with a calibration target. The position and orientation of the target were obtained by a registration process. The selection of the target shape and size was found to be critical to a successful calibration at sea, due to the limitations in the manoeuvrability of the ROV.

Keywords: calibration; laser profiling; image correction; registration; sediment roughness; microtopography.

1. Introduction

In shallow water acoustics measurements seafloor roughness affects high-frequency acoustic scattering. It is therefore advantageous to be able to characterize the micro-topography of the seafloor so that it can be accounted for in the analysis of received acoustic signals. Several methods have been developed to measure seafloor roughness including stereophotogrammetry, laser profiling, and the use of conductivity probes. For this application, the general objective is to achieve a resolution of the order of 1 mm or better, with a swath width greater than one meter. In pattern recognition circles, the laser profiling method is known as structured light, and there are a few publications concerning its underwater application (e.g., Salvi *et al.* 2004 and Gupta, *et al.* 2011).

The calibration process described in this paper was developed for a laser profiling system (Chotiros *et al.* 2007, Varghese and Isakson 2005). This system, diagrammed in Fig. 1, consists of a digital camera and an arrangement of six red lasers that are spread into parallel planes by cylindrical lenses. The intersection of these planes with the seafloor creates profiles of the local topography that are recorded by the digital camera and processed to form a topographical map of the scanned area. Although only one laser would suffice, using six lasers effectively produces multiple measurements of the same area and improves accuracy. During processing, points of intersection

*Corresponding author, Research Scientist, E-mail: chotiros@arlut.utexas.edu

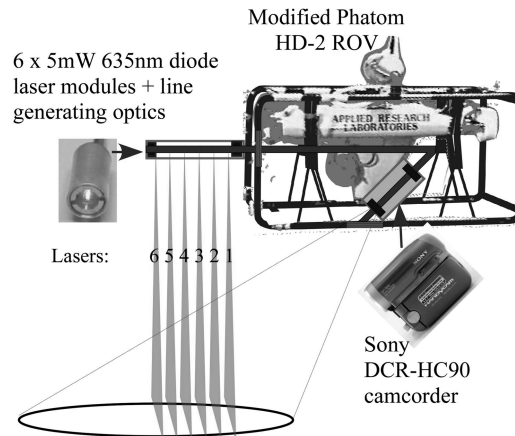


Fig. 1 Laser profiling system

between the scanned surface and the laser planes are extracted from the 2D digital image and transformed into 3D space according to the equations of the intersecting planes. Because the system calibration determines both the laser plane equations and the 2D image coordinates, the accuracy of the topographical map depends heavily on the quality of the calibration.

Compared to other recent devices used to measure the microtopography of the seafloor, the laser profiler described in this paper has several advantages. First, the profiler is steered remotely so it is easier to use than systems that require divers to move and operate equipment. Compared to frame-mounted laser imaging systems (Jaffe 2005, Wang Hefner and Tang 2009), the ROV mounted profiler can image a larger area of the seafloor, although resolution is affected by the moving frame of reference. Second, using a video camcorder, rather than a still camera (Lyons *et al.* 2002, Wang and Tang 2009), a faster sampling rate hence a higher area coverage rate is obtained. Third, since the system is hosted in a ROV, there is no mechanical contact with the seafloor, which is a very important consideration when working in protected areas where disturbance of the seafloor is forbidden. Finally, the profiler is relatively inexpensive because it uses an off-the-shelf digital camcorder. There are similar systems mounted on autonomous underwater vehicles (AUV), but they use only one laser beam (Bodenmann *et al.* 2010, Kondo *et al.* 2004 and Sangekar *et al.* 2010). The use of multiple lasers increases the coverage rate and improves accuracy.

A two-stage calibration was performed. In the first stage, image distortions were directly corrected and an undistorted virtual camera that followed the pinhole camera model was constructed (Cumani and Guiducci 1995). After the correction was made, a simple trigonometric transform was all that was necessary to project from the three-dimensional world into the two-dimensional image coordinate systems. In the second stage, laser plane equations were determined using a calibration target of known geometry. Compared to other calibration techniques, the procedures described here are simple and versatile. A target-based calibration of an underwater laser scanner by Wang and Cheng (2007), depends on the accuracy of the camera's lens geometry and the precise placement of the laser. The method described here is more robust, allowing for distortions in the image and changes in the laser/camera alignment. A major goal in the development of this calibration process was to find a method that would be relatively easy to implement each time measurements were taken in the field. Performing repeated field calibrations for the device is necessary because each

time the profiling system is assembled at the testing location, the alignment of the camera and lasers may change. The calibration process has been designed with attention to efficiency, flexibility, and simplicity.

In the next section, the first stage of the process, the image distortion correction, is described. Then, the second stage, the laser plane estimation process, is described, including the design and selection of the calibration targets. In section 4, the results of a calibration process are shown. Finally, conclusions are drawn. The selection of the target shape and size and its registration in 3D, were found to be critical.

2. Virtual camera construction

The virtual camera was modeled in two steps. Given the (x,y) coordinates in a camera image, x and y error maps were calculated and used as the basis for an interpolation based image-warping transform. Then the optical center and focal distance of a distortion-free virtual camera representing the entire camera/housing/water arrangement were calculated.

2.1 Distortion correction

The camera used in the laser profiling system is an off-the-shelf Sony DCR-HC96 camcorder housed in a waterproof case with a plexiglass window. When the camera is filming underwater, light rays that travel from an object must cross the water/window interface, the window/air interface, then pass through the camera lenses before reaching the camera's sensor plane. These multiple interfaces combined with mild misalignments that may occur within the camera or within the camera casing cause the digital image to be distorted. Due to the irregularity of the distortion, calibration techniques that strive to find a specific function to fit the radial and tangential distortions (Weng *et al.* 1992, Yu 2003 and Tsai 1987) will not suffice. Instead, the distortion was modeled as a black box process where the input and output are the only important parameters. The key assumption is that the distortion is repeatable. That is, for every set of three-dimensional input data, the camera always produces an image that is distorted in the same pattern. This is a valid assumption, given the static arrangement of the camera within its housing and the fact that spatial variations in the refractive index of sea water (Quan and Fry 1995) are negligible under normal water conditions. This approach also corrects for distortions that exist in consumer grade cameras, for which strict standards of accuracy are not guaranteed. It is logistically easy to implement, as it does not require precision equipment that would be difficult to deploy underwater.

The distortion was measured through the use of a test grid to generate a distorted/ideal image pair from which x and y error maps in the image space could be created. The test grid was a 0.61×1.21 m (2×4 feet) planar stainless steel rectangle onto which 0.635 cm (0.25 inch) diameter black dots had been placed at 2.54 cm (1 inch) horizontal and vertical intervals, in a regular grid pattern. In a test tank, an underwater image of the test grid was captured. For this image, the camera/housing assembly was positioned so that the image plane of the camera was parallel to the test grid plane. The x and y image coordinates of the grid points (black dots) were extracted from the test image. Then, using the grid points in the center of the image as a rough positional reference and taking advantage of the regular point geometry of the test grid, a grid of ideal point positions was computed. For every measured grid point, the x and y error relative to the ideal grid was calculated

and indexed to its pixel position in a large two-dimensional array containing an index for every pixel in the test image (720×480 pixels in this case). Polynomial curves were fit horizontally and vertically to the rows and columns in the error arrays and used to interpolate a specific correction for each pixel in the test image. Fig. 2 is a graphical representation of the x and y pixel errors.

The distorted/ideal image pair is shown in the lower left panel in Fig. 3. Two guide grids with densely packed points evenly distributed across the image space were generated—one of which was subsequently distorted according to the calculated x and y pixel errors. The guide grids were passed as reference inputs to an image warping interpolation algorithm to correct the distortion. The guide grids, and examples of uncorrected and corrected grid images are displayed in Fig. 3.

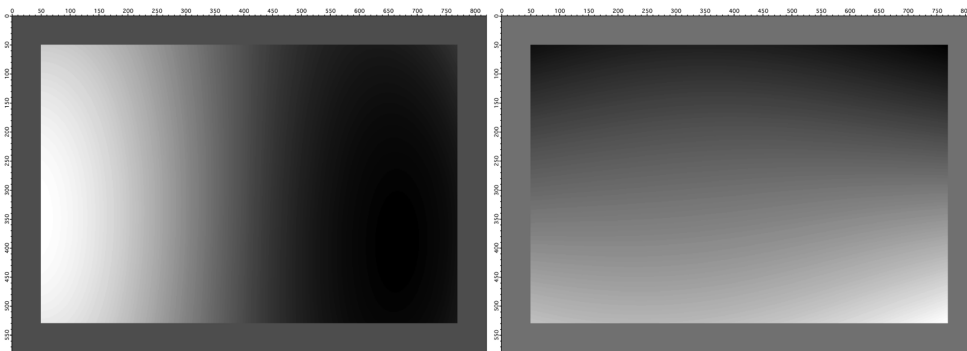


Fig. 2 The x -(left) and y - (right) errors represented as grayscale images. The darkest regions of the image correspond to the most negative error and the lightest regions of the image correspond to the most positive error. The gray band around each image is a buffer

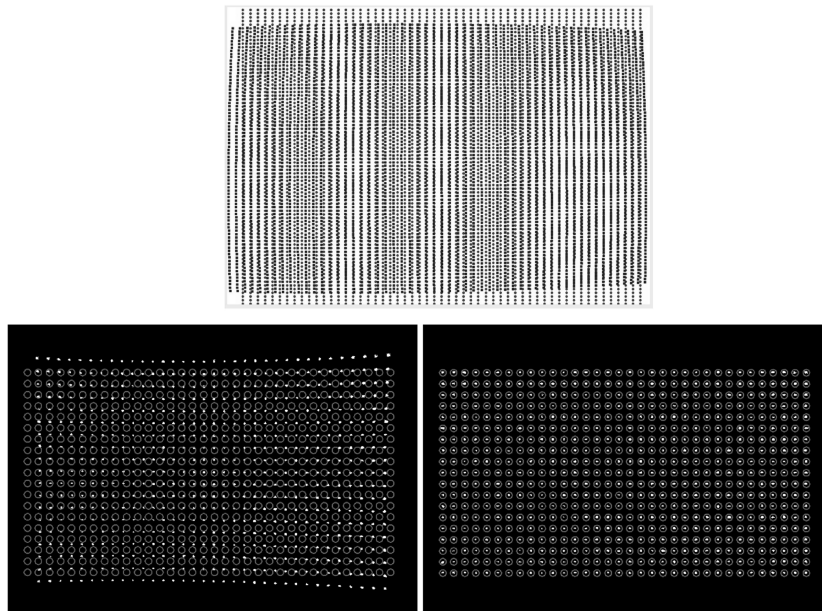


Fig. 3 The interpolation grids (top): original (red) and target (blue) positions, and the uncorrected (left) and corrected (right) grid images (white dots) compared to the target image (red circles)

2.2 Camera parameter estimation

In the pinhole camera model, a Cartesian “world” coordinate system (x_w, y_w, z_w) with the optical center of the virtual camera at the origin and the x -axis extending along the camera’s forward axis, may be projected into 2-dimensional image coordinates (x_{im}, y_{im}) according to the following formulae

$$x_{im} = \frac{y_w}{x_w}f + C_{imx} \quad (1)$$

$$y_{im} = \frac{z_w}{x_w}f + C_{imy} \quad (2)$$

where f is the focal distance of the virtual camera in pixels, and (C_{imx}, C_{imy}) is the center image pixel.

To find the focal length of the virtual camera, images of the same test grid were captured at eleven distances from an arbitrary origin. The images were corrected using the interpolation grids and the separation between adjacent grid points (dots) in each image was measured. Based on the pinhole camera model embodied in the above equations, the separation between grid points in the image space should tend to infinity as the distance from the test grid to the optical center tends to zero. Using this relationship, the offset distance was determined by plotting the inverse grid point separation in image space against the measured distance to the test grid, as shown in Fig. 4. The intercept of the best-fit straight line with the distance axis indicated the offset. The linearity of the plot was important as it both validated the assumption that the distortion of the camera arrangement was repeatable and indicated how well the virtual camera fit the pinhole camera model. For a perfect fit the points would be precisely linear. In this experiment a coefficient of determination of

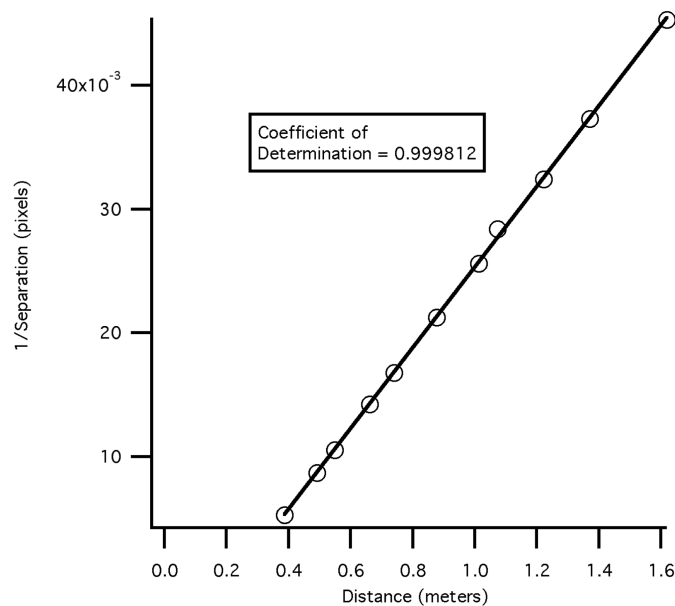


Fig. 4 Inverse grid point separation in image space as a function of distance

0.999812 was measured for the linear regression of the eleven data points.

The focal length of the virtual camera was determined according to the simple relationship

$$f = \frac{aX}{A} \quad (3)$$

where f is the focal distance, a the grid point separation in the image in pixels, X the corrected distance to the test grid, and A the physical grid point separation (one inch). A focal distance for each data point was calculated and the results were averaged to determine the best estimate focal distance.

3. Laser plane determination

To determine the equations of the laser planes, the image coordinates of the intersection points between the laser planes and a calibration target were measured. Three different objects were tested as calibration targets: a tent, a bounded plane, and a cylindrical “top hat”. Example video frames showing the intersection of the laser planes with each target are shown in Fig. 5. The ideal calibration target needed to meet several criteria. Because precise movements are difficult to execute with the ROV to which the profiling system is attached, the calibration target needed to be approachable from multiple angles and heights to make data collected from field calibrations more robust. Also, determining the laser planes requires that the equations of the surfaces they intersect be known, so limiting the complexity of the calibration target surfaces eases computation. Finally, when calibration videos are taken, the object should provide a sufficient distribution of laser/object intersection points to produce accurate plane equation estimates by means of a least-squares error fitting process.

The calibration process was carried out using each calibration target. For each target, a 3D computer model was created based on its geometry and projected into the 2D image space. In the registration process, the model position and orientation were adjusted to match the projected image to the recorded one. This registration provided known surfaces from which 3D points in each laser plane could be found. This process was carried out with several video images until a significantly large data set of 3D laser plane points had been generated. Because the lasers and camera system move as a single unit, the 3D cloud of data points naturally segmented itself into six groups

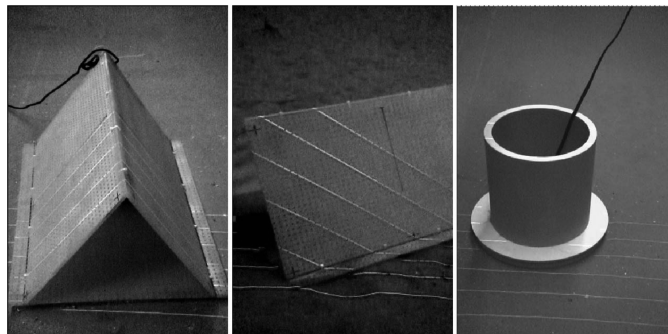


Fig. 5 Calibration targets: tent (left), bounded plane–rectangle defined by the black crosses (center) and top-hat (right)

corresponding to the six laser planes. These groups were separable and a plane was fitted to each group of points using a least-squares error fitting algorithm.

The major differences between the calibration targets concerned the registration process. The plane and tent were registered by minimizing of the sum of squared differences between reference points, typically corners, in the projected computer model and corresponding points in the digital image. This method proved to be less accurate than desired. For the tent, reference points from the digital image were difficult to locate precisely because of poor contrast. For the plane, frames in which the target plane was nearly parallel to the image plane could not be accurately registered because the pixel coordinates of the reference points were relatively insensitive to small rotations. For both objects, the pixel coordinates of the reference points in each image had to be manually identified, which introduced human error and was time consuming.

The top-hat object was designed to mitigate the problems found with the bounded plane and tent targets. The top-hat has two 2 plane surfaces and it was painted to specifically highlight those surfaces. The painting also made it possible to isolate the object from its surroundings by thresholding, which allowed the registration process to be automated. Registering the top-hat was done by a simulated annealing algorithm in which the parameter to be maximized was the cross-correlation peak between the object in the image and an image mask made from the computer model of the object. To prepare the target image for registration, a Laplacian of the Gaussian edge detector was used to locate the object in the image. Then an image mask of the 3D model was created with points along the circular edges of the object. Parameters to adjust the rotation and translation of the 3D model were then passed to the simulated annealing function and the best-fit world position of the object in the image was found. An example of the registration result is shown in Fig. 6(left). Following this process, the planar faces of the top-hat were calculated from the model.

After registering the top-hat, laser/target intersection points were extracted from the image using

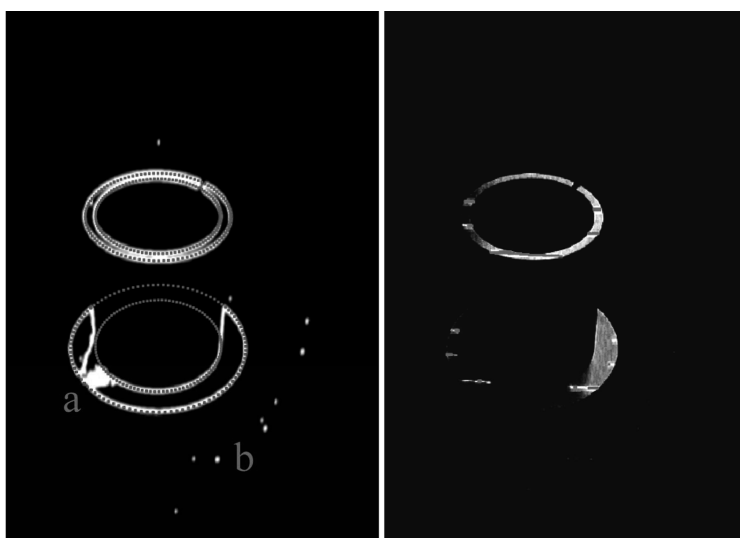


Fig. 6 Left: Identified object edges (white) and the registered position of the computer model (red dots): (a) distortions in the processed image due to shadows and (b) light colored debris in the background. Right: Identified laser/object intersection points (red)

color and adaptive thresholding techniques, an example of which is shown in Fig. 6 (right). Using the top-hat planes, laser points from the image were projected into 3D coordinates according to the following formulae. Each target plane may be represented by a simple plane equation

$$x = a + by + cz \quad (4)$$

where a , b , and c are known coefficients. The ray angles corresponding to image coordinates (x_{im}, y_{im}) are given by

$$\tan(\theta_y) = \frac{(x_{im} - C_{imx})}{f} \quad (5)$$

$$\tan(\theta_z) = \frac{(y_{im} - C_{imy})}{f} \quad (6)$$

The ray intersects the target plane at the 3D world coordinates

$$x_w = \frac{a}{(1 - b \tan(\theta_y) - c \tan(\theta_z))} \quad (7)$$

$$y_w = x_w \tan(\theta_y) \quad (8)$$

$$z_w = x_w \tan(\theta_z) \quad (9)$$

By processing multiple frames in this manner, using all available target planes, a 3D cloud of points for each laser plane was generated. In the x - z plane, the natural segmentation of the points

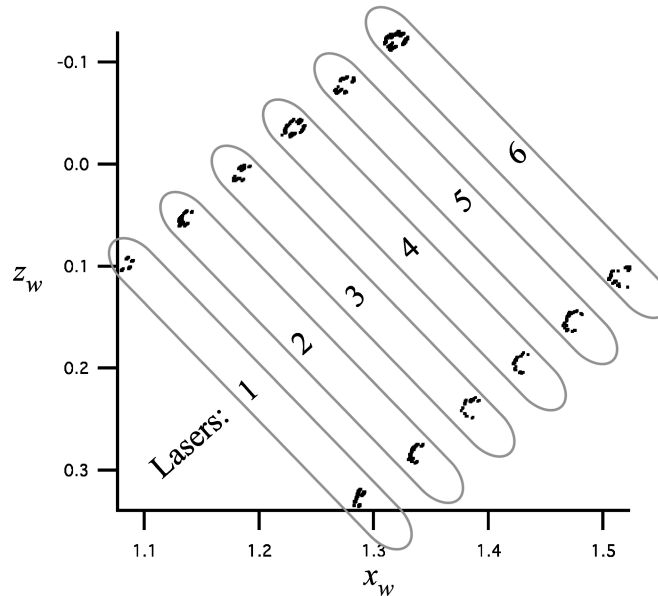


Fig. 7 Coordinates of laser points projected on to the x - z plane. Clouds of points are separable and color-coded by laser plane. Cloud width due in part to laser planes not perfectly perpendicular to x - z plane

Table 1. Laser plane coefficients

	Laser 1	Laser 2	Laser 3	Laser 4	Laser 5	Laser 6
<i>a</i>	0.996	1.083	1.171	1.256	1.3409	1.416
<i>b</i>	-0.061	-0.060	-0.072	-0.068	-0.083	-0.076
<i>c</i>	0.873	0.874	0.858	0.846	0.852	0.835

into groups is apparent, as illustrated in Fig. 7. For each laser, two sub-groups are identifiable, one for each of the two target planes. A least-squares error plane fit was computed for each group to yield the laser plane coefficients.

4. Results

The estimated plane coefficients for the six laser planes using the top-hat target are shown in Table 1. These values were calculated from laser/object intersection points collected from 11 video frames. The *a* values indicate where each laser plane intersects the *x*-axis and the *b* and *c* values relate to rotations about the *y*- and *z*-axes, respectively. These plane coefficients are consistent with the geometry of the profiling system and indicate nearly parallel laser planes with a slight negative rotation about the *y*-axis and an approximate 40 degree tilt relative to the camera's forward *x*-axis – the average value of *c* is 0.8563 which is equal to the tangent of 40.57 degrees.

The error in the laser plane coefficients may contain systematic and random components. Any residual distortion in the imaging system will contribute to the systematic component. The random component is expected to come from random errors in the registration of the calibration target. Of the three calibration targets used, the top-hat target gave the lowest standard deviation in the rotational plane parameters *b* and *c*, indicating the least amount of random error, and the best registration performance. The standard deviations of both the *b* and *c* values corresponded to a standard deviation in angle of 0.5 degrees. Since each pair of sub-groups in Fig. 6 has a physical separation of approximately 0.3 m, the standard deviation in angle corresponds to a standard deviation in position of around 3 mm. Since this was obtained by averaging the results from 11 video images, assuming that the random errors are independent zero-mean processes, the random component of calibration error may be reduced by increasing the number of images. The objective of a 1 mm standard deviation may be achieved by increasing the number of measurements by a factor of 9, e.g., from 11 video frames to 99.

5. Conclusions

A calibration process for an underwater laser profiling system was developed. Compared to more traditional land-based calibration techniques, this method minimizes external measurements that are difficult to make accurately when the device is being calibrated in the field, particularly when deployed on a ROV underwater. The calibration is divided into two stages: (a) The camera distortion was measured and corrected, using a virtual pinhole camera model. The virtual camera model both corrects for irregular distortions and allows for conversion between 2D image and 3D world coordinates without precise knowledge of the physical camera's internal parameters. (b) The positions of the laser planes relative to the camera were measured with the aid of a calibration

target. The position and orientation of the calibration target was obtained by a registration process. The points at the intersection of the laser and target planes in image space were projected into 3D space to produce point clouds, from which the laser plane coefficients were estimated. The design of the calibration target was critical. It had to have plane surfaces for simplicity in calculating the laser intersection points. It had to be usable from any direction because its azimuthal orientation relative to the ROV is often difficult to control in an underwater environment, due to the limited manoeuvrability of the ROV. Finally, its shape has to be amenable to automatic registration in a robust manner. These qualities were achieved with the top-hat target design. In the future, a more accurate device will be developed using a camera with high-definition capabilities and green lasers that give crisper images.

Acknowledgments

Video footage of the tent and top-hat targets were made in the test tank of the Applied Research Laboratories, The University of Texas at Austin (ARL:UT). Video footage of the bounded-plane target was from the Measurement and Analysis of the Relationship between the Environment and Sonar or Synthetic Aperture Sonar performance (MARES) joint experiment between the NATO Undersea Research Centre (NURC) and ARL:UT. The authors wish to acknowledge the ARL:UT team, projector leader Marcia Isakson and ROV pilot James Piper, and the outstanding cooperation by NURC, Mario Zampolli, chief scientist, Captain Andrea Iacono and the crew of the RV Leonardo, Gaetano Canepa and the Engineering Coordinator Per Arne Sletner for assistance in many areas.

References

- Bodenmann, A., Thornton, B., Ura, T., Sangekar, M.N., Nakatani, T. and Sakamaki, T. (2010), "Pixel based mapping using a sheet laser and camera for generation of coloured 3D seafloor reconstructions", *Proceedings of the Oceans*, Sydney, Australia, May.
- Chotiros, N.P., Isakson, M.J., Piper, J.N. and Zampolli, M. (2007), "Seafloor roughness measurement from a ROV", *Proceedings of the Proc. International Symposium on Underwater Technology*, Tokyo, Japan, April.
- Cumani, A. and Guiducci, A. (1995), "Geometric camera calibration: the virtual camera approach", *IEEE T. Consum. Electr.*, **8**(6), 375-384.
- Gupta, M., Agrawal, A., Veeraraghavan, A. and Narashimhan, S.G. (2011), "Structured light 3D scanning in the presence of global illumination", *Proceedings of the Proc. 24th IEEE Conference on Computer Vision and Pattern Recognition*, Colorado Springs, USA, June.
- Jaffe, J.S. (2005), "Performance bounds on synchronous laser line scan systems", *Proceedings of the Oceans05 Europe*, Brest, France, June.
- Kondo, H., Maki, T., Ura, T., Nose, Y., Sakamaki, T. and Inaishu, M. (2004), "Relative navigation of a autonomous underwater vehicle using a light-section profile system", *Proceedings of the IEEE/RSJ International Conference on Intelligent Robots and Systems*, Sendai, Japan, 28 September - 2 October.
- Lyons, A.P., Fox, W.L.J., Hasiotis, T. and Pouliquen, E. (2002), "Characterization of the two-dimensional roughness of wave-rippled sea floors using digital photogrammetry", *IEEE J. Oceanic Eng.*, **27**(3), 515-524.
- Quan, X. and Fry, E.S. (1995), "Empirical equation for the index of refraction of seawater", *Appl. Optics*, **34**(18), 3477-3480.
- Salvi, J., Pagés, J. and Batlle, J. (2004), "Pattern codification strategies in structured light systems", *Pattern Recog.*, **37**(4), 827-849.

- Sangekar, M.N., Thornton, B., Nakatani, T. and Ura, T. (2010), "Development of a landing algorithm for autonomous underwater vehicles using laser profiling", *Proceedings of the Oceans*, Sydney, Australia, May.
- Tsai, R.Y. (1987), "A versatile camera calibration technique for high-accuracy 3D machine vision metrology using off-the-shelf TV cameras and lenses", *IEEE T. Robot. Auto.*, **3**(4), 323-344.
- Varghese, S.M. and Isakson, M.J. (2005), "The calibration of a laser light line scan method for determining local interface roughness of the ocean floor", *IEEE J. Oceanic Eng.*, **30**(2), 463-467.
- Wang, C.C. and Cheng, M.S. (2007), "Nonmetric camera calibration for underwater laser scanning system", *IEEE J. Oceanic Eng.*, **32**(2), 383-399.
- Wang, C.C. and Tang, D. (2009), "Seafloor roughness measured by a laser line scanner and a conductivity probe", *IEEE J. Oceanic Eng.*, **34**(4), 459 - 465.
- Wang, C.C., Hefner, B.T. and Tang, D. (2009), "Evaluation of laser scanning and stereo photography roughness measurement systems using a realistic model seabed surface", *IEEE J. Oceanic Eng.*, **34**(4), 466-475.
- Weng, J., Cohen, P. and Herniou, M. (1992), "Camera calibration with distortion models and accuracy evaluation", *IEEE T. Pattern Anal.*, **14**(10), 965-980.
- Yu, W. (2003), "An embedded camera lens distortion correction method for mobile computing applications", *IEEE T. Consum. Electr.*, **49**(4), 894-901.